Fluorescent molecular rotors

From working principles to visualization of mechanical contacts

Suhina, T.

2

Experimental Methods and Data Analysis

Abstract

This chapter describes experimental methods and data analysis procedures that are used in this thesis. The chapter is divided in three sections; the first section describes steady-state spectroscopy, the second one time-resolved spectroscopy, and the final section describes microscopy. Each section includes the description of the instrument and of data analysis. The spectroscopic methods consist of steady-state absorption (UV-vis, FTIR) and emission, picosecond time-resolved fluorescence (Time Correlated Single Photon Counting, TCSPC), femtosecond vis-pump/vis(mid-IR) probe experiments, confocal microscopy and fluorescence lifetime imaging techniques.

2.1 Steady-state measurements

Steady-state measurements are performed under constant illumination and observation. In this type of experiments the sample is illuminated with a continuous beam of light, while the intensity of transmitted (absorption) or emitted (emission) light is being recorded. Due to very short timescales on which absorption (almost momentary) and emission (ps or ns) of light occurs, the system usually reaches the stationary state promptly. This way, time-averaged spectra are obtained.[1] Throughout this work, steady-state measurements have been used to extract both qualitative and quantitative information.

2.1.1 Instrumentation

Electronic absorption spectra were measured with a Shimadzu UV-2700 spectrophotometer.

All fluorescence excitation and emission spectra were recorded using a SPEX Fluorolog 3-22 fluorimeter, which is equipped with double grating monochromators in both the excitation and emission channels. A 450 W Xenon lamp was used for excitation, and a Peltier cooled R636-10 (Hamamatsu) photomultiplier tube was used for detection of the emitted light. Spectra of the liquid samples were collected in a right-angle geometry, while the spectra of the solid samples (cover slips) were collected in the front face geometry. All the measured spectra were corrected for the spectral sensitivity of the instrument and light intensity fluctuations (unless otherwise noted).

2.1.2 Fluorescence quantum yields

The fluorescence quantum yield is one of the most important characteristics of a chromophore. It is the ratio between the number of emitted and absorbed photons.[1] All fluorescence quantum yields (Φ_f) reported in this thesis are determined using the relative quantum yield measurement method.[2,3] This method is based on comparison between the integrated emission of the sample and the integrated emission of the standard sample for which the quantum yield value is known. The fluorescence spectra are measured under the same experimental conditions, for solutions of known absorbance values at the excitation wavelength.[3] Before integration, reference and sample spectra are corrected by solvent background subtraction. The fluorescence quantum yield of the sample is then calculated according to Eq. 2.1.

$$\Phi_{\mathrm{f,x}} = \Phi_{\mathrm{f,st}} \frac{F_\mathrm{x}}{F_\mathrm{st}} \frac{f_\mathrm{st}}{f_\mathrm{x}} \left(\frac{n_\mathrm{x}}{n_\mathrm{st}} \right)^2 \tag{2.1}$$

In this expression, $\Phi_{\mathrm{f,x}}$ is the fluorescence quantum yield of the sample, $\Phi_{\mathrm{f,st}}$ is fluorescence quantum yield of the standard, F_x is the integrated emission of the sample, F_st is the integrated emission of the standard, f_x is the absorption factor (where $f = 1 - 10^{A}$, A being the absorbance at the excitation wavelength) of the sample, f_st is the absorption factor of the standard, n_x is the refractive index

of the solvent of the sample, and n_{st} is the refractive index of the solvent of the standard solution.

2.1.3 Estimation of radiative decay rate constants from the Strickler-Berg equation

The radiative decay rate of a molecule can be estimated from the Strickler-Berg expression (see Eqs. 2.2 and 2.3).[4]

$$k_{\mathrm{rad}} = 2.88 \times 10^{-9}\ n^2\ \tilde{\nu}_{em}^3 \int_{S_1} \frac{\epsilon(\nu)}{\nu} d\nu \tag{2.2}$$

$$\tilde{\nu}_{em}^3 = \frac{\int F(\nu) d\nu}{\int F(\nu)\nu^{-3} d\nu} \tag{2.3}$$

In this expression, $F(\nu)$ and $\epsilon(\nu)$ are the emission and absorption spectrum (on a cm^{-1} scale), respectively, and n is the refractive index of the medium. The natural lifetime can be obtained according to Eq. 2.6. Although this expression holds rather well for a large number of cases,[1,4] it does not account for possible changes in the excited-state electronic structure and specific interactions between the chromophore and the solvent. Throughout this thesis, we often use this expression to check whether significant changes in the excited-state electronic structures take place. If significant changes in excited-state electronic structure do not occur, electronic transition dipole moments for the absorption and emission are expected to be equal ($M_{01} = M_{10}$). Electronic transition moments for absorption and emission can be obtained via Eqs. 2.4 and 2.5, respectively.[5]

$$M_{01} = 9.58 \times 10^{-2} \sqrt{\frac{1}{n} \int_{S_1} \frac{\epsilon(\nu)}{\nu} d\nu} \tag{2.4}$$

$$M_{10} = 1.786 \times 10^{3} \sqrt{\frac{k_{\mathrm{rad}}}{n^3 \tilde{\nu}_{em}^3}} \tag{2.5}$$

$$\tau_{\mathrm{n}} = \frac{1}{k_{\mathrm{rad}}} \tag{2.6}$$

2.1.4 Model for reversible TICT state formation under steady-state conditions

The following model will be used in Chapter 5, where we measure fluorescence intensities of a fluorescent molecular rotor as a function of temperature. It will enable us to monitor relative changes in nonradiative rate as a function of temperature. This model describes the case where the fluorescent locally excited state (P) is formed upon photoexcitation of the ground-state (GS), and reversibly converts to the (dark) Twisted Intramolecular Charge Transfer State (T). It was originally proposed by Grabowski[6] and adjusted by Dreger in ref. 7 for the fluorescence

response of molecular rotors in polymer matrices under pressure. The model assumes steady-state conditions and is schematically shown in Scheme 2.1. Here,

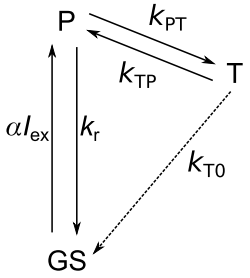

Scheme 2.1: Schematic representation of the reversible TICT state formation model discussed in the text.

α represents a fraction of the photons absorbed, I_{ex} is the intensity of the excitation light, k_r is the decay rate of the locally excited state, k_{PT} and k_{TP} are rates of interconversion between the locally excited and twisted states, and k_{T0} is the twisted state deactivation rate. The decay of the locally-excited state k_r represents mainly the contribution from radiative process, as a contribution from internal conversion is much smaller in these compounds.[7,8] In this model, k_r is assumed to be temperature-independent. The situation depicted in Scheme 2.1 can be expressed by the following rate equations:[7]

$$\partial[P]/\partial t = \alpha I_{ex} - (k_r + k_{PT})[P] + k_{TP}[T] \tag{2.7}$$

$$\partial[T]/\partial t = k_{PT}[P] - (k_{TP} + k_{T0})[T] \tag{2.8}$$

Because only the locally excited state (P) is fluorescent, fluorescence intensity can be expressed by Eq. 2.9. This allows us to compare intensities (quantum yields) at different temperatures which is expressed by Eq. 2.10. Here, $X = k_{PT}k_{T0}/(k_{TP} + k_{T0})$ and all variables are assumed to show temperature dependence. The temperature effect will then mainly be reflected in the ratio between $X(T_x)/X(T_{ref})$. This can be expressed in terms of either rate constants or fluorescence quantum yields, as shown in Eq. 2.11[7] where $r(T_x) = \Phi_f(T_x)/\Phi_f(T_{ref})$.

$$I = k_r[P] = \frac{\alpha I_{ex} k_r}{k_r + k_{PT}k_{T0}/(k_{TP} + k_{T0})} \tag{2.9}$$

$$\frac{I(T_x)}{I(T_{ref})} = \frac{\Phi_f(T_x)}{\Phi_f(T_{ref})} = \frac{1 + X(T_{ref})/k_r}{1 + X(T_x)/k_r} \tag{2.10}$$

$$\frac{X(T_x)}{X(T_{ref})} = \frac{k_{PT}(T_x)\ k_{T0}(T_x)}{X(T_{ref})\ (k_{TP}(T_x) + k_{T0}(T_x))} = \frac{1 - r(T_x)\,\Phi_f(T_{ref})}{r(T_x)\ (1 - \Phi_f(T_{ref}))} \tag{2.11}$$

2.1.5 Solvatochromism

The molecular rotors examined in this work manifest a high degree of charge-transfer character upon photoexcitation (with an exception of the BODIPY based rotor discussed in Chapter 6), which results in a highly polar excited state. As the solvent polarity increases, such polar excited states become increasingly stabilized through interactions with the solvent molecules, and the energy difference between the ground and excited states becomes smaller.

Since molecular rotors are usually more polar in their excited state than their ground state, solvent stabilization has a larger influence on their emission energies than on absorption energies. In addition, the larger effect on emission energies stems from the relaxation of the molecule and the solvent, which takes time, and cannot occur during the excitation process. This manifests itself in larger differences between the electronic absorption and emission energies, which is measured as the Stokes shift, as the environment polarity increases.[1,9] Solvatochromism is commonly described by the Lippert-Mataga equation, in which Stokes shifts are expressed as a function of solvent orientational polarization.[10,11] In its commonly used form, this model ignores specific solute-solvent interactions, and it only considers the polarization induced in the solvent by the fixed ground and excited-state dipoles. The influence of the solute polarizability is taken into account in the polarizable point dipole dielectric continuum model, where the solvent's orientational polarization function ($\Delta f = \frac{\epsilon_r - 1}{2\epsilon_r + 1} - \frac{n^2 - 1}{2n^2 + 1}$) is replaced with $d_c(\epsilon_r) - d_c(n^2)$.[12–14]

$$\bar{\nu}_{abs} - \bar{\nu}_{em} = \frac{2}{hc}[d_c(\epsilon_r) - d_c(n^2)]\frac{(\vec{\mu}_{ES} - \vec{\mu}_{GS})^2}{a^3} + constant \tag{2.12}$$

$$d_c(x) = \frac{d_0(x)}{1 - 2cd_0(x)} = \frac{x - 1}{2(1 - c)x + (1 + 2c)} \tag{2.13}$$

$$d_0(x) = \frac{x - 1}{2x + 1} \tag{2.14}$$

The model is defined by Eqs. 2.12-2.14, where $\bar{\nu}_{abs}$ and $\bar{\nu}_{em}$ are electronic absorption and emission energies, h is Planck's constant, c is the speed of light, a is the solute cavity radius, n is refractive index of the solvent, ϵ_r is relative permitivitty of the solvent, and μ_{GS} and μ_{ES} are ground and excited-state dipole moments, respectively. Parameter c is related to solute polarizability α, and it can vary between $c = 0$ (non-polarizable limit) and c = 0.5. For c = 0, $d_c(x) = (x - 1)(2x + 1)$ and $d_c(\epsilon_r) - d_c(n^2)$, the same as the solvent's orientational polarization expression ($\Delta f = \frac{\epsilon_r - 1}{2\epsilon_r + 1} - \frac{n^2 - 1}{2n^2 + 1}$) from the Lippert-Mataga equation.[10,11] In this work, we calculate the values of c via $c = \alpha/a^3$. Both α and a can be estimated from DFT calculations. The difference between the ground and excited-state dipole moment can then be calculated from the line slope by plotting the measured Stokes shifts (in cm^{-1}) *vs* $d_c(\epsilon_r) - d_c(n^2)$.

2.2 Time-resolved measurements

Steady-state measurements can indisputably provide a wealth of information about the chromophores and their excited-state dynamics. In spite of their usefulness, the nature of these experiments limits the amount of information that can be extracted. Due to constant illumination conditions, the ground and excited-state populations rapidly reach steady-state conditions. As a consequence, the obtained signal is time averaged and a part of the information is lost. Time-resolved measurements enable us to obtain non-averaged signals, which makes it possible to extract information which is lost under the steady-state conditions.

The basis of most time-resolved experiment is perturbation of the ground-state molecular population by a short light pulse which causes a sudden increase in the excited-state population. The signal produced by the excited-state population after the excitation pulse is then monitored as a function of time. This signal can, for example, be fluorescence intensity (as in time correlated single photon counting) or difference in absorption of the sample after and before the laser pulse (transient measurements). Through (occasionally quite complex) modeling of such data, a wealth of information about the examined system can be obtained. Time-resolved measurements are used throughout this thesis to examine the excited-state dynamics of molecular rotors.

2.2.1 Time correlated single photon counting

Instrument description

Time correlated single photon counting monitors fluorescence intensity of the sample after the laser pulse as a function of time. The setup used to conduct these experiments is schematically shown in Fig. 2.1. Excitation light (450-488 nm, vertically polarized) is generated by frequency doubling of the output of a fully automatic tunable Ti:sapphire laser (Chameleon Ultra, Coherent; $P \sim 2400$ mW @ 830 nm; $f = 80$ MHz). Laser output is in some cases used to pump an optical parametric oscillator (Mira OPO PP-Automatic, Coherent) in order to produce the required wavelength (530 nm). The repetition rate of the laser is decreased from the fundamental frequency of $f = 80$ MHz to $f = 8$ MHz using a pulse picker (PulseSelect, APE). After passing the second harmonic generation (SHG), the excitation light is split from the "reference" light using a dichroic mirror (DM). When the OPO is used, SHG is removed and a beam splitter is used instead of a dichroic mirror. The excitation light (typically $\sim$1 mW) is used for sample excitation, while the "reference" light is guided through a delay line towards the fast photodiode (PD). Fluorescence from the sample is gathered under the magic angle conditions and focused towards the multichannel plate photomultiplier tube (MCP, Hamamatsu R3809U-50 or Hamamatsu R3809U-51) through a single-grating monochromator (M20, Carl Zeiss, 600 lines/mm or an ORIEL Cornerstone 260 mm). Although the excitation source produces sub-picosecond pulses, due to electronics and detector, a typical instrument response function (IRF) of this setup has full width at half maximum of $\sim$ 25 ps. The IRF is obtained either

by measuring a dilute scattering solution (Ludox) or reflections from a ceramic plate at the excitation wavelength. In order to maximize the photon collecting efficiency of the instrument, the emitted photon is used as a "start" signal for voltage ramp build-up in the time-to-amplitude converter (TAC). The voltage is built up until a "reference" photon reaches the PD, which produces "stop" signal. The produced voltage is then converted to a corresponding arrival time by an multi-channel analyzer (MCA) and added to the decay histogram in the computer (PC).[1,15]

TCSPC data analysis

TCSPC data in this thesis are analyzed either by means of a set of in-house built IgorPro macros or using DecFit,[16,17] a Python-based software package written by Nikolai V. Tkachenko. The principles for analysis of the time-resolved fluorescence data are shortly described below.

The simplest case scenario can be expressed as $[GS]_0 \xrightarrow{\delta} [ES](t) \xrightarrow{k_0} [GS](t)$ ($[ES](t=0) = [ES]_0 \ll [GS]_0$), in which an infinitely short (δ-function) laser pulse brings a fraction of the total ground-state fluorophore population $[GS]_0$ in the solution to the (fluorescent) excited state (see Fig. 2.2). Excited-state

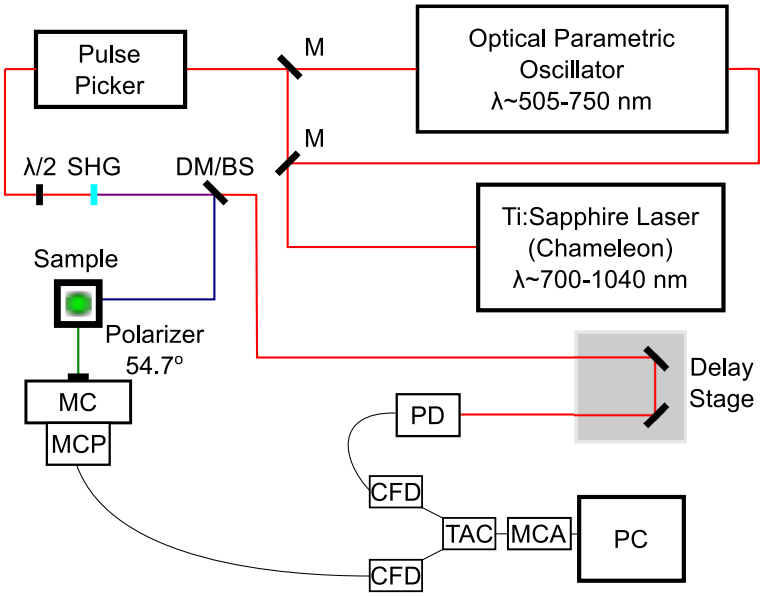

Figure 2.1: Schematic representation of the TCSPC setup in our lab. M = flipping mirrors, $\lambda/2$ = half-wave plate, SHG = second harmonic generator, DM = dichroic mirror, BS = beam splitter, MC = monochromator, MCP = multichannel plate, PD = photodiode, CFD = constant fraction discriminator, TAC = time-to-amplitude converter, MCA = multichannel analyser.

population will decay according to:

$$\frac{\partial[ES](t)}{\partial dt} = -k_0[ES](t) \tag{2.15}$$

where $[ES](t)$ is the concentration of the fluorophore in its excited state at time t and k_0 is the sum of the rate constants that lead to the excited-state deactivation. The fluorescence signal we measure by TCSPC, $I(t)$, is directly proportional to the concentration of the fluorophore in its excited state, $[ES](t)$. Integration of Eq. 2.15 gives an exponential function (Eq. 2.16):

$$I(t) = I_0 \exp(-t/\tau_0) \tag{2.16}$$

where I_0 represents fluorescence emission at $t = 0$ and $\tau_0 = 1/k_0$ is the fluorescence lifetime. Integrating this expression will give the steady-state intensity, $I_0\tau_0$ (at the wavelength where the decay was measured).

Fluorescence decays are often not single exponential. Excited-state species might undergo excited-state reactions, or multiple fluorophores might be present. Corresponding fluorescence decay curves are then described by:

$$I(t) = \sum_{i=1}^{n} \alpha_i \exp(-t/\tau_i). \tag{2.17}$$

In Eq. 2.17, α_i is the pre-exponential factor of the i^{th} component, n is the number of components, and τ_i is the corresponding lifetime. When multi-exponential decays are present it is often useful to calculate the average fluorescence lifetime (τ_{avg}), which is defined as:

$$\tau_{\text{avg}} = \sum_{i=1}^{n} \frac{\alpha_i \tau_i^2}{\alpha_i \tau_i} \tag{2.18}$$

Equations 2.16 and 2.17 represent the so-called impulse response functions,[1] which are not observed under the experimental conditions. In reality, laser pulses are not infinitely short, and more importantly, the characteristic properties of electronics and detectors cause a significant spread in the impulse response functions. This results in "smearing", or convolution of the measured fluorescence decay signals and impacts the time resolution of such experiments. The "smearing" effect is usually estimated by measuring excitation light from the scattering samples, for example a diluted ludox solution, which provides a good estimate on convolution of a δ-function due to the setup characteristics. This information is referred to as instrument response function (IRF) and presents an important factor for time resolution. The effect of IRF on measured fluorescence decays is illustrated in Fig. 2.2 on some simulated data.

Throughout this thesis, we use a measured (or in some cases assumed) IRF in order to increase the accuracy of data analysis. This is especially important when fluorescence lifetimes approach the time resolution of the instrument. Under realistic conditions, the measured signal can be expressed as a convolution integral:

$$S(t) = \int_0^t R(t')I(t-t')dt' \tag{2.19}$$

where $S(t)$ is the measured signal, $R(t)$ is the measured (or simulated) instrument response function, and $I(t)$ is the ideal response of the sample (infinitely short excitation pulse and instrument response).[1,18] If the sample response is expressed as a sum of exponentials, the signal measured at a particular wavelength can be expressed as:

$$S(t,\lambda) = \sum_{i=1}^{n} \alpha_i(\lambda) \int_0^t R(t')\exp(-\frac{t-t'}{\tau})dt' \tag{2.20}$$

This function is then used to fit the measured data: the measured (or assumed) IRF (R) is iteratively convolved with the assumed sample response model (impulse response function), and $(S_{\mathrm{exp}}(t,\lambda) - S_{\mathrm{calc}}(t,\lambda))^2$ is then minimized by the non-linear least squares method. Although this process is technically re-convolution, it is often referred to as deconvolution. If needed, Eq 2.20 can be modified to account for scattered excitation light (or Raman). This is done by adding the term $\alpha_{IRF}R(t')$ to Eq. 2.20, which is δ-pulse response convolved with the instrument response ($R(t')$) and scaled by a factor α_{IRF} (additional fitting parameter).

If certain conditions are met (photon collection times are the same and spectral sensitivity of the detection is accounted for), integrals of the measured decay curves $\int_{t=0}^{\infty} S(t,\lambda)$ plotted against the wavelengths at which they were measured would reproduce the steady-state spectrum. Conducting such measurements, combined with instrument response "deconvolution" allows us to obtain both spectral and kinetic data, and becomes especially powerful when combined with global analysis, described below.

Global analysis combines multiple experiments in which some parameters are shared for all experiments (global), and the other ones are optimized independently for each individual experiment. For instance, fluorescence decays can be measured at multiple wavelengths and fitted by requiring that fluorescence lifetimes are simultaneously optimized for all measurements. This way, we would obtain a set of amplitudes (pre-exponential factors) associated with the respective fluorescence lifetimes for each individual measurement (at a particular wavelength). Often,

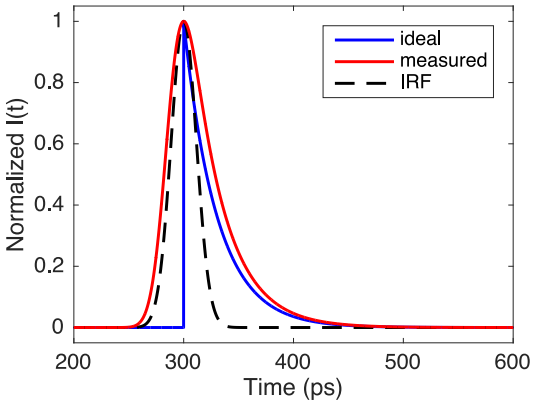

Figure 2.2: Due to non-ideal instrument response (black) on δ-function pulse, the observed fluorescence decay (red) differs from the sample response (blue) which would be observed under the ideal conditions (infinitely short excitation pulse and instrument response).

measured fluorescence decays show multiexponential behavior and in such situations kinetic parameters associated with individual components are difficult (or sometimes even not possible) to resolve by fitting of the individual curves.[1] Both parameter discrimination and accuracy of the parameter recovery can be dramatically enhanced by simultaneous (global) analysis of multiple datasets, which are obtained under slightly different conditions (different monitoring wavelengths, for example). In the simplest case of a mixture of two non-interacting fluorophores (which exhibit a single exponential decay) in a solution, the respective fluorescence lifetimes of the two fluorophores would be defined as global (wavelength independent) parameters, while their respective amplitudes would be optimized as wavelength-dependent variables according to Eq. 2.20. Global fitting then yields the (wavelength independent) fluorescence lifetimes of the two fluorophores, and their amplitudes as a function of the wavelength at which they were obtained. Plotting the amplitudes multiplied by lifetimes *vs* wavelength yields the decay associated fluorescence spectra (DAFS), which ideally correspond to the steady-state spectra of the two individual fluorophores. In practice, however, optical components and detectors have different spectral sensitivities for different wavelengths and this needs to be accounted for. One way to correct for the spectral sensitivity is to measure a known fluorescence standard and use it for calibration of the spectral sensitivity of the setup. This is often not a preferred choice, as a large number of photons tends to be collected near the maximum of the emission or spectral sensitivity of the equipment, while the edges tend to have only a few photons detected under constant photon collection times. The preferred method is to optimize the instrumental settings for each wavelength and use the corrected steady-state spectrum to normalize the fitted decay traces. The area under each fluorescence decay curve corresponds to the steady-state emission intensity, which can be used to calculate the wavelength-dependent correction factors:

$$area = \int_{t=0}^{\infty} I(t,\lambda) = \int_{0}^{\infty} \alpha_i(\lambda)\, \exp(-t/\tau_i)dt = \sum_{i=1}^{n} \alpha_i(\lambda)\tau_i, \tag{2.21}$$

$$correction(\lambda) = \frac{F(\lambda)}{area}, \tag{2.22}$$

where $F(\lambda)$ is the corrected steady-state intensity for the monitoring wavelength λ. The decay associated fluorescence spectra of the respective components is then reconstructed by expression:

$$\mathrm{DAFS}_i(\lambda) = correction(\lambda) \times \alpha_i \times \tau_i. \tag{2.23}$$

As mentioned previously, in case of non-interacting excited-state species (as in a solution containing the mixture of two non-interacting fluorophores), the reconstructed spectra correspond to the spectra of the individual fluorophores and are described as species associated fluorescence spectra. Since fluorophores often undergo excited-state reactions, where relationships between the excited-state species can be complex, the decay associated spectra do not represent the spectra of the

individual species. The interpretation of such decay associated spectra becomes non-trivial, and more advanced compartmental global analysis methods discussed later in this chapter need to be employed in order to extract the physically meaningful parameters.

2.2.2 Femtosecond transient measurements

Transient data described in this thesis are analyzed with Glotaran[19] (Java-based guided used interface for the R package TIMP[20]) and Matlab equipped with Ultrafast toolbox.[21] A brief description of the fitting methods is provided below.

Transient spectroscopy methods monitor changes in a sample absorption ($\Delta A(\lambda, t)$) after perturbation by a laser pulse (pump) as a function of time:

$$\Delta A(\lambda, t) = A_{\mathrm{p}}(\lambda, t) - A_{\mathrm{np}}(\lambda, t), \tag{2.24}$$

where $A_{\mathrm{p}}(\lambda, t)$ and $A_{\mathrm{np}}(\lambda, t)$ represent the absorption spectra at time t of the sample with and without perturbation by the pump pulse, respectively. The sample absorption is defined as the negative logarithm of the transmission T of the sample:

$$\Delta A(\lambda, t) = -\log_{10} T_{\mathrm{p}}(\lambda, t) + \log_{10} T_{\mathrm{np}}(\lambda, t), \tag{2.25}$$

where $T_{\mathrm{p}}(\lambda, t)$ and $T_{np}(\lambda, t)$ represent sample transmissions with and without the pump pulse, respectively. Transmission of the sample is defined as the intensity ratio of the probe with ($I^{probe}(\lambda, t)$) and without ($I_0^{probe}(\lambda, t)$) the light passing through the irradiated sample:

$$\begin{aligned} \Delta A(\lambda, t) &= -\log_{10}\left(\frac{I_{\mathrm{p}}^{probe}(\lambda, t)}{I_{0,\mathrm{p}}^{probe}(\lambda, t)}\right) + \log_{10}\left(\frac{I_{\mathrm{np}}^{probe}(\lambda, t)}{I_{0,\mathrm{np}}^{probe}(\lambda, t)}\right) \\ &= -\log_{10}\left(\frac{I_{\mathrm{p}}^{probe}}{I_{\mathrm{np}}^{probe}}\right). \end{aligned} \tag{2.26}$$

Since the intensity of the probe can not be measured simultaneously for the presence and the absence of the pump pulse, an identical copy of the probe pulse which passes through the part of the sample that remains unaffected by the pump pulse is used as a reference ($I_0^{probe}(\lambda, t)$). The use of a reference minimizes shot-to-shot laser pulse fluctuations and increases signal-to-noise ratio of the measurement. In our vis-pump/mid-IR probe setup, the signal is obtained this way. Alternatively, a reference pulse can be obtained by measuring the probe-pulse with a chopper synchronized in a way to block the pump-pulses. The measured signal is then:

$$\Delta A(\lambda, t) = \frac{I(t)_n^{pump}}{I(t)_{n+1}^{probe}}, \tag{2.27}$$

where n represents number of the pulse, $I(t)_n^{pump}$ intensity of the transmitted light with pump and $I(t)_{n+1}^{probe}$ intensity of the transmitted light with probe only. In our

vis-pump/vis-probe setup, for example, probe runs at 1 kHz, while the pump runs at 500 Hz (regulated with chopper) and transient signal is obtained according to the Eq. 2.27. We use the first method to record signal in our vis-pump/mid-IR, and the second one in vis-pump/vis-probe measurements.

Instrument description

Vis-pump/vis-probe Experiments: Femtosecond transient absorption experiments were performed with a Spectra-Physics Hurricane Ti:Sapphire regenerative amplifier system with a repetition rate of 1 kHz, wavelength 800 nm. Visible pump pulses (478 nm or 488 nm, ∼0.45-1.5 μJ pulse (<200 fs fwhm, estimated from pump-probe cross-correlation)) were generated by sum-frequency mixing the Ti:sapphire pump and an signal of an optical parametric amplifier (OPA) in a BBO crystal. 5% Of the fundamental light was used for white light continuum generation from 350 nm to 850 nm, by focusing on a CaF_2 plate. This serves as a probe pulse. A Berek Polarizer (New Focus) was included in the setup to provide the magic-angle conditions of the polarizations of pump and probe light. The probe light was twice passed over a delay line (Physik Instrumente, M-531DD) that provides an experimental time window of 3.6 ns. The samples were placed in cells of 2 mm path length (Hellma). The absorption spectra were detected with a 150 mm spectrograph (Princeton Instrument SP2150 with a 300 lines/mm grating) and a single diode-array (Hamamatsu NMOS S3901-512Q). The readout was done using fast electronics (TEC5). A chopper running at 500 Hz was used to measure a reference (non-pumped) signal by blocking half of the pump pulses. The transient spectra were obtained from the non-pumped transmitted intensity and the pumped transmitted intensity spectra.

Vis-pump/mid-IR probe Experiments: Tunable visible pump and mid-IR probe pulses were generated using a Ti:sapphire laser (Spectra-Physics Hurricane, 600 μJ pulse). Pump pulses at 488 nm were generated by sum-frequency mixing the Ti:sapphire pump and the signal of a BBO-based OPA (pulse energy was $\sim 3\mu$J); IR probe/reference pulses were generated by difference-frequency mixing the signal and idler from a second OPA in $AgGaS_2$ and reflected off the front and back surfaces of the BaF_2 window. The sample cell with CaF_2 windows spaced by 500 μm was placed in the IR focus. Using a Newport ESP300 translation stage, the delay positions were scanned by mechanically adjusting the beam path of the vis-pump. A temporal resolution of 200 fs was estimated from the fwhm of the pump-probe cross-correlation function. The transient spectra were obtained by subtracting non-pumped absorption spectra from the pumped absorption spectra that were recorded by a custom built 30-pixel double array MCT detector coupled to an Oriel MS260i spectrograph.

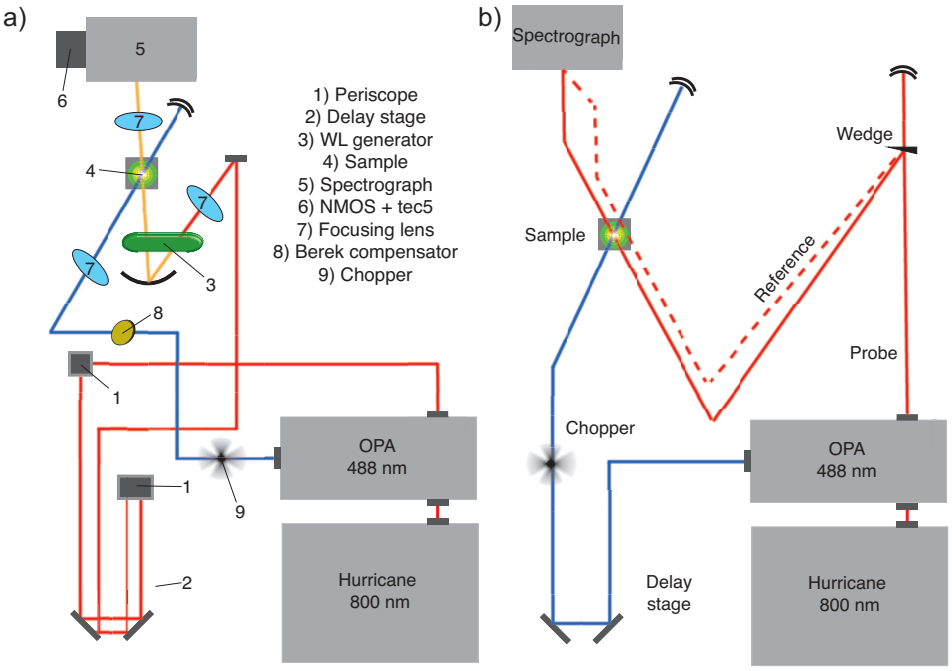

Figure 2.3: Simplified schematic representation of a) vis-pump/vis-probe experimental setup; b) vis-pump/mid-IR probe experimental setup.

Data analysis: parallel model

Since the transient data is usually collected for a large number of wavelengths simultaneously, global analysis of the transient matrix is usually employed to extract meaningful information. The procedure is analogous to the one described for the global analysis of the fluorescence decays. The measured curves can be expressed as:

$$\Delta A(t,\lambda) = \sum_{i=1}^{n} \alpha_i(\lambda) \int_0^t R(t')\exp(-\frac{t-t'}{\tau})dt', \tag{2.28}$$

and iterative reconvolution of the sample response function with the instrument response function can be used to obtain relevant parameters. In this work, the instrument response for the transient data analysis is approximated as a gaussian function. Global analysis of the transient matrix yields respective amplitudes as a function of wavelength ($\alpha_i(\lambda)$), from which the decay associated difference (DADS) spectra can be directly reconstructed by plotting the amplitudes of individual components *vs* their respective wavelengths. In the case of transient measurements time traces do not need to be normalized (as in the case of fluorescence decays), because the signal in the presence of the pump pulse is measured relative to the signal in the absence of the pump pulse. As in the case of fluorescence decays,

these spectra would represent the species associated difference spectra in the simple case of non-interacting species present in solution. If this is not the case, so-called compartmental global analysis with an assumed model is used to obtain the relevant spectral and temporal parameters.

Data analysis: compartmental global analysis and singular value decomposition

In many cases, excited-state transformations with mutual dependence between the excited-state species occur during the measurement. When such dependence exists, DADS do not represent the true spectra of the involved species. In order to reconstruct the spectra associated with individual species, a quantitative model for time dependencies of the relevant species (or some other constraints) needs to be assumed. Measured spectra at each wavelength can be written as:

$$\Delta A(\lambda, \{t\}) = \sum_{i=1}^{n_{species}} S_i(\lambda) M(\{t\}, \{P\}), \tag{2.29}$$

in which transient spectra at wavelength λ is expressed as a linear combination of the individual species spectra ($S_i(\lambda)$) and their concentrations in time (defined by a model, $M(\{t\}, \{P\})$), which are dependent on the set of model parameters P. The set of transient spectra (A) measured at different times and wavelengths can be arranged into a $n_\lambda \times n_t$ data frame matrix $\mathbf{DF}$, which can be expressed as:

$$\mathbf{DF} = \mathbf{SM}(\{P\}), \tag{2.30}$$

where $\mathbf{DF}$ is a $n_\lambda \times n_t$ data matrix, $\mathbf{S}$ is a $n_\lambda \times n_{species}$ matrix of species spectra, and $\mathbf{M}(\{P\})$ is a $n_{species} \times n_t$ matrix. Each column of $\mathbf{DF}$ is the spectra measured at time t, each column of $\mathbf{S}$ represents the spectrum associated with one of the $n_{species}$ species, and each row of $\mathbf{M}$ represents time dependent concentration of one of the $n_{species}$ species. The task of compartmental analysis is to determine the optimal set of parameters $\{P\}$ and matrix $\mathbf{S}$ of species associated spectra which satisfy Eq. 2.30. From this point, the unknowns are, at least in principle, obtainable by treating each of the amplitudes and model parameters as independent adjustable parameters. In practice, the sheer amount of the adjustable parameters (all spectral amplitudes are treated as independently adjustable parameters) makes the convergence difficult and unreliable. One of the ways to tackle this issue is by complete orthogonal decomposition[22] of the matrix $\mathbf{M}$, or variable projection, which are employed in order to reduce the number of adjustable parameters.[23] For instance, TIMP uses a refined version of variable projection referred to as partitioned variable projection.[20] Detailed description of all variable projection algorithms falls outside of the scope of this overview, and the reader is referred to the specialized literature.[20,22–24] Instead, we will shortly discuss an approach based on singular value decomposition (SVD), due to its wide usability (not only in spectroscopy), noise removal properties, and overall relative simplicity.[24]

SVD can dramatically facilitate the data fitting process due to its ability to reduce the number of parameters that need to be estimated by the least squares algorithm.[24,25] The main idea of SVD is that the $n_\lambda \times n_t$ ($n_\lambda > n_t$) matrix $\mathbf{DF}$ can be expressed as a product of three matrices:

$$\mathbf{DF} = \mathbf{U\Sigma V'} = \sum_{i=1}^{N} \sigma_i \mathbf{u}_i \mathbf{v'}_i, \tag{2.31}$$

where $\mathbf{U}$ is the $n_\lambda \times n_t$ projection matrix, $\mathbf{\Sigma}$ is a $n_t \times n_t$ diagonal matrix which contains non-negative diagonal elements (σ_i) called singular values of $\mathbf{DF}$, and $\mathbf{V}$ is a $n_t \times n_t$ matrix.[24–26] The columns of $\mathbf{U}$ and $\mathbf{V}$ represent sets of orthonormal vectors, such that $\mathbf{UU'} = \mathbf{VV'} = \mathbf{I}$; where $\mathbf{I}$ represents a $n_t \times n_t$ identity matrix and the sign $'$ means that the matrix is transposed. The columns of $\mathbf{U}$ are the projection vectors $\mathbf{u}_i$ ($n_\lambda \times 1$ sized vectors), called the basis spectra of $\mathbf{DF}$. The time dependence of the individual basis spectra to each of the measured spectra ($\mathbf{DF}$ columns) is given in the rows of $\mathbf{V'}$, $\mathbf{v'}_i$ ($1 \times n_\lambda$ sized vectors). The measured dataset can thus be decomposed into the outer sum of $\mathbf{u}_i\mathbf{v'}_i$ weighted by the corresponding singular values in $\mathbf{\Sigma}$, $\boldsymbol{\sigma}_i$. The singular values contained in a diagonal matrix $\mathbf{\Sigma}$ are ordered from high to low, where the highest values have the largest contributions.[25] This means than one can then only take n components associated with the highest singular values and reconstruct the reduced data matrix $\mathbf{DF}_{\mathrm{red}}$ which only contains components with significant contributions:

$$\mathbf{DF} \approx \mathbf{DF}_{\mathrm{red}} = \mathbf{U}_{red}\mathbf{\Sigma}_{red}\mathbf{V'}_{red} = \sum_{i=1}^{n} \sigma_i \mathbf{u}_i \mathbf{v'}_i. \tag{2.32}$$

This process instantly reduces the number of components ($n < N$, n is number of components after SVD, N is the number of components before SVD) that we need to include in our fitting in order to obtain concentrations and spectra of the individuals species of interest. As the added benefit, a significant amount of noise is removed, as the noise components tend to be associated with lower singular values. It is assumed that all measured spectra can be represented as linear combinations of the columns of $\mathbf{U}_{red}$. From this point, for simplicity, we will use notation of $\mathbf{DF}$, $\mathbf{\Sigma}$ and $\mathbf{V}$ for the reduced datasets obtained as described above.

For any square invertible $n \times n$ matrix ($\mathbf{CC}^{-1} = \mathbf{I}$), it is possible to write:

$$\mathbf{DF} = \mathbf{UCC}^{-1}\mathbf{\Sigma V'} = \mathbf{SM}, \tag{2.33}$$

where $\mathbf{S} = \mathbf{UC}$, and $\mathbf{M} = \mathbf{C}^{-1}\mathbf{\Sigma V'}$.[26,27] Matrix $\mathbf{S}$ ($n_\lambda \times n$) contains basis spectra, and $\mathbf{M}$ ($n \times n_t$) contains target vectors. In order to extract the species associated spectra, coefficients contained in matrix $\mathbf{C}$ need to be determined. This is either done by imposing constraints on the basis spectra and/or target vectors, or by assuming a specific kinetic model.[24] For the cases where the constraints are not available, the transformation matrix $\mathbf{C}$ can be obtained by the least squares fit of:

$$\mathbf{CM} = \mathbf{\Sigma V'}, \tag{2.34}$$

where $\mathbf{M}$ has a form:

$$\mathbf{M} = \begin{pmatrix} N_{species_1}(t_1) & N_{species1}(t_2) & \dots & N_{species1}(t_{n_t}) \\ N_{species_2}(t_1) & N_{species2}(t_2) & \dots & N_{species2}(t_{n_t}) \\ \dots & \dots & \dots & \dots \\ N_{species_n}(t_1) & N_{species_n}(t_2) & \dots & N_{species}(t_{n_t}) \end{pmatrix}, \tag{2.35}$$

that is defined by the assumed model.

2.3 Fluorescence microscopy

In this thesis, all contact area images were obtained by confocal microscopy. SymPhoTime software (provided with the instrument) was used for fluorescence decay fitting in order to obtain fluorescence lifetime images. The individual time traces were either fitted with IgorPro, DecFit, or Matlab. Due to difficulties with instrument response estimation, deconvolution was avoided if possible. In this section we will briefly describe the working principle of a confocal microscope, and some very basic principles of digital image processing.

2.3.1 Instruments

Confocal microscopy is a fluorescence imaging technique, which means that it allows us to monitor fluorescence from the samples. A simplified confocal microscopy setup is schematically shown in Fig. 2.4. The collimated light source (laser in our case) is spectrally filtered with an excitation filter, which is required if the laser light is not purely monochromatic. The excitation light is reflected from the dichroic mirror and travels towards the objective, which focuses it on the sample. The fluorescence from the sample is then collected and collimated by the objective, and passes the dichroic mirror and emission filter, which eliminates residual reflected light passed through by the dichroic. The fluorescence light then travels towards the pinhole, which eliminates a large amount of out-of-focus fluorescence, and is collected on the detector (which is in our case either PMT or SPAD, for Zeiss and PicoQuant microscopes, respectively). The pinhole that eliminates out of focus fluorescence is the main advantage of confocal over wide-field imaging.

The contact area measurements were made using a confocal microscope (Zeiss Axiovert 200M) and a microscope control system (Pascal). Excitation was at 488 nm (or 530 nm), and emission was monitored by a combination of adequate dichroic mirrors and filters. The objective used was a 63× 1.3 NA (plan-apochromat, Zeiss). Spheres were glued to the tool of an Anton Paar DSR 301 rheometer that was used to apply and control the normal force on the contact. A schematic illustration of this experiment can be found in Fig. 1.5. The images were analyzed in MatLab and Fiji (ImageJ).

Fluorescence lifetime images were measured with a MicroTime 200 confocal microscope (PicoQuant GmbH) based on an Olympus IX-71 microscope body and a 100× 1.4 NA objective (UplanSApo, Olympus), mounted on a piezo-scanning

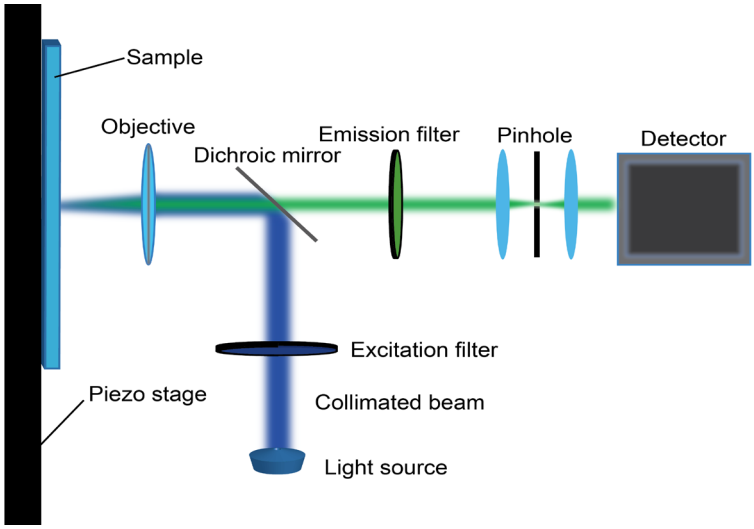

Figure 2.4: Simplified schematic representation of a confocal microscope.

stage (Physik Instruments GmbH). A detection pinhole with a diameter of 50 or 75 μm was used. An NKT Photonics SuperK Extreme Supercontinuum white laser (80 MHz) was used as the excitation source. The working principle of the fluorescence lifetime imaging microscope is identical to the one described previously for the fluorescence imaging microscope, with the notable difference that a time correlated single photon counting unit is incorporated into the setup. The working principle of TCSPC can be found in Section 2.2.1. The MicroTime 200 box with its components is shown in Fig. 2.5.

Confocal images are obtained by scanning, measuring luminescence in one point at a time. By moving the focused light (either by moving the laser or the sample) across the sample, the sample is scanned in the x-y plane. This process can be repeated for different sample planes (z-planes), which results in a three dimensional image of the object. The time that the objective spends collecting photons at a certain location is called pixel dwell time. Longer dwell times mean that more photons are collected, which result in less noise due to averaging. While morphological properties of an image can be determined with relatively few photons (tens of photons) per point, this is not the case in fluorescence lifetime imaging, which requires a larger number of photons in order to fit the obtained decay curves reliably.[28] Long dwell times, however, lead to photobleaching of the sample so measurement parameters often need to be optimized for the individual samples.

2.3.2 General considerations and data analysis

Resolution of a confocal microscope

The resolution of a fluorescence microscope represents its ability to resolve two closely separated objects. If a very small object ($\ll \lambda$) is being imaged, its interaction with light will result in formation of a characteristic diffraction pattern known as Airy disk, which results in blurring of such small objects. The size of such a pattern is larger than the object that is being imaged. The radius of the Airy disk is given by:[29]

$$R = \frac{0.61\lambda}{NA}, \tag{2.36}$$

where R is radius of the Airy disk, λ is the wavelength of monitored light, and NA is the numerical aperture of the objective. Two objects are considered to be separable if their distance is equal to or larger than the Airy disk radius, which is known as the Rayleigh criterion. The radius of the Airy disk for 1.4 NA objective and monitored wavelength of 530 nm is $R = 230$ nm, which means that two objects are separable if they are located at least 230 nm one from another. This principle is illustrated in Fig. 2.6, where the Airy function has been generated using the Born and Wolf model implemented in Fiji.[30] The Airy disk is two dimensional, but blurring in microscope occurs in three dimensions and the amount of blurring is defined by a point spread function (PSF) of the microscope. Since confocal microscopy uses point-wise illumination (PSF_{exc}) and detection (PSF_{em}), only the fluorophores within the shared illumination/detection volume ($\mathrm{PSF}_{exc} \times \mathrm{PSF}_{em}$)

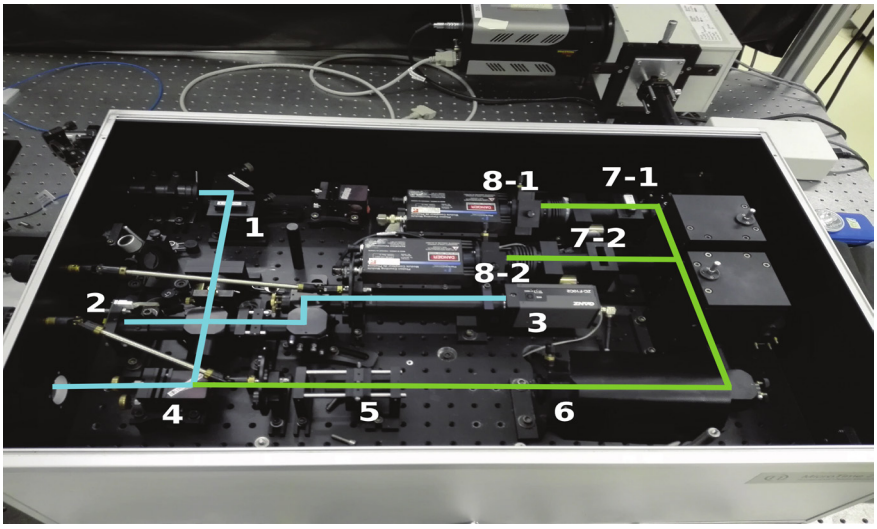

Figure 2.5: MicroTime 200 unit of PicoQuant fluorescence lifetime imaging confocal microscope: **1** = excitation filter, **2** = photodiode, **3** = CCD, **4** = dichroic, **5** = tubelens, **6** = pinhole, **7-1** and **7-2** = emission filters, **8-1** and **8-2** = SPADs.

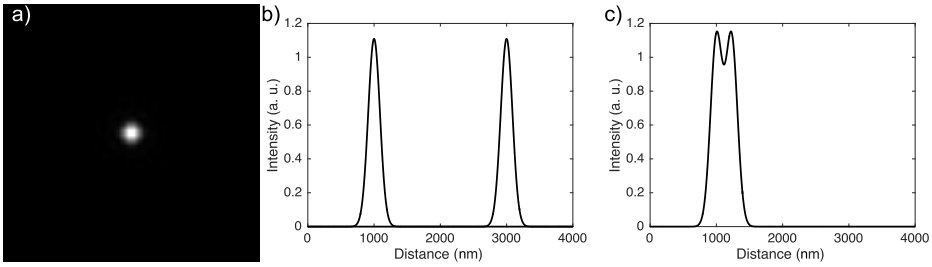

Figure 2.6: Resolving two objects under a fluorescence microscope. a) Simulated Airy disk for 1.4 NA objective and 530 nm monitored wavelength; b) Simulated intensity profile of two well separated objects; 3) Simulated intensity profile of two objects separated sufficiently to be considered resolvable.

can be detected. The spatial resolution of a confocal setup therefore differs from the resolution of a wide-field microscope. Under the assumption that both PSF_{exc} and PSF_{em} have gaussian shapes, the lateral resolution of a confocal microscope can be approximated with:[29,31]

$$R \approx \frac{0.4\ \lambda_{em}}{NA}. \tag{2.37}$$

This theoretical limit should not be confused with resolution of a confocal microscope working under practical conditions, as ideal conditions that are assumed in theoretical PSF estimation are not possible to achieve in practice (signal-to-noise ratio is not infinite, optical aberrations are often present, "pixelation"-division of an image into finite structural elements upon image digitalisation , imperfections in index matching are often present,...). This often results in resolution that is significantly worse than the one predicted by theory. Both resolution and the contrast of the image can be increased by performing deconvolution with the measured (or estimated) PSF. Discussion about microscopy deconvolution algorithms lies out of the scope of this overview, and the reader is referred to the specialized literature, such as ref. 30 and the references therein.

Data analysis

Contact Area Measurements

Microscopy images were quantitatively analyzed using *in house* built scripts in Matlab. The analysis included image pre-processing, *e.g.* filtering in order to reduce the amount of Poissonian noise from the data. This was achieved either by applying median or gaussian filters, where the kernel size was optimized for each image (depending mainly on the pixel size of a particular measurement). Although median filter is generally preferred for noise removal purposes, the application of the gaussian filter did have a significant impact on our spatial resolution since the pixel size ($\sim$ 100 nm) was kept below the experimentally determined optical resolution of our system ($300 - 450$ nm, depending on objective and pinhole size).

After noise reduction, the images were thresholded (binarized) using the Otsu thresholding method.[32] In short, this method assumes that the image contains a bimodal pixel distribution of foreground (in our case contact) pixels and background (non-contact) pixels. The algorithm then attempts to find the optimal number (threshold) by minimizing (or, equivalently, maximizing) their combined spread. Pixels below the obtained value then assume the value of 0, and pixels above the obtained value assume the value of 1.[32] The obtained matrix of zeroes and ones can then be used to calculate the contact area.

Since the pixel size of the obtained image known, a size scaling factor can be obtained. The number of pixels that contain "true" signal (all pixels in thresholded image with the value of 1) can then simply be summed up and multiplied by the scaling value to give the measured contact area.

Fluorescence Lifetime Imaging

Fluorescence lifetime imaging differs from the conventional, purely intensity based imaging in a way that a fluorescence decay curve is associated with each of the measured pixels. In other words, for a 250 by 250 pixels image, 62500 fluorescence decay curves are collected. Each of these curves can be fitted with a model (usually monoexponential or multiexponential functions) to obtain the fluorescence lifetime image. Fluorescence lifetime imaging holds some obvious advantages which make it more robust than the intensity-based imaging, as fluorescence lifetimes are not dependent on fluorophore concentration (except in cases such as self-quenching and re-absorption), photobleaching, absorption or the thickness of the sample.

In the case of our contact measurements, fitting the fluorescence decays within the contact area with mono or biexponential models produced unsatisfactory fit qualities for many pixels. For this reason, we have calculated the average lifetime with the fast FLIM procedure.[33] This procedure calculates "average lifetime" values as the average photon arrival times after the laser pulse.

References

1. Lakowicz, J. R. *Principles of Fluorescence Spectroscopy*; Springer Science & Business Media, 2006.
2. Brouwer, A. M. *Pure Appl. Chem.* **2011**, *83*, 2213–2228.
3. Würth, C.; Grabolle, M.; Pauli, J.; Spieles, M.; Resch-Genger, U. *Nat. Protoc.* **2013**, *8*, 1535–1550.
4. Strickler, S.; Berg, R. A. *J. Chem. Phys.* **1962**, *37*, 814–822.
5. Lewis, J.; Maroncelli, M. *Chem. Phys. Lett* **1998**, *282*, 197–203.
6. Grabowski, Z. R.; Rotkiewicz, K.; Rettig, W. *Chemical reviews* **2003**, *103*, 3899–4032.
7. Dreger, Z.; Lang, J.; Drickamer, H. *Chem. Phys.* **1992**, *166*, 193–206.

8. Willets, K. A.; Callis, P. R.; Moerner, W. *J. Phys. Chem. B* **2004**, *108*, 10465–10473.
9. Reichardt, C.; Welton, T. *Solvents and solvent effects in organic chemistry*; John Wiley & Sons, 2011.
10. Mataga, N.; Kaifu, Y.; Koizumi, M. *Bull. Chem. Soc. Jpn.* **1956**, *29*, 465–470.
11. Lippert, E. *Ber. Bunsenges. Phys. Chem.* **1957**, *61*, 962–975.
12. Arzhantsev, S.; Zachariasse, K. A.; Maroncelli, M. *J. Phys. Chem. A* **2006**, *110*, 3454–3470.
13. Dahl, K.; Biswas, R.; Ito, N.; Maroncelli, M. *J. Phys. Chem. B* **2005**, *109*, 1563–1585.
14. Jin, H.; Liang, M.; Arzhantsev, S.; Li, X.; Maroncelli, M. *J. Phys. Chem. B* **2010**, *114*, 7565–7578.
15. Becker, W. *Advanced time-correlated single photon counting techniques*; Springer Science & Business Media, 2005; Vol. 81.
16. Lehtivuori, H.; Efimov, A.; Lemmetyinen, H.; Tkachenko, N. V. *Chem. Phys. Lett.* **2007**, *437*, 238–242.
17. Lehtivuori, H.; Kumpulainen, T.; Efimov, A.; Lemmetyinen, H.; Kira, A.; Imahori, H.; Tkachenko, N. V. *J. Phys. Chem. C* **2008**, *112*, 9896–9902.
18. O'Connor, D.; Ware, W.; Andre, J. *J. Phys. Chem.* **1979**, *83*, 1333–1343.
19. Snellenburg, J.; Laptenok, S.; Seger, R.; Mullen, K.; Van Stokkum, I. *J. Stat. Softw.* **2012**, *49*.
20. Mullen, K. M.; Van Stokkum, I. H. *J. Stat. Softw.* **2007**, *18*, 1–46.
21. van Wilderen, L. J.; Lincoln, C. N.; van Thor, J. J. *PLoS One* **2011**, *6*, 17373.
22. Lawson, C. L.; Hanson, R. J. *Solving least squares problems*; SIAM, 1995.
23. Golub, G.; Pereyra, V. *Inverse Probl.* **2003**, *19*, R1.
24. Henry, E. R. *Biophys. J.* **1997**, *72*, 652–673.
25. Press, W. H.; Teukolsky, S. A.; Vetterling, W. T.; Flannery, B. P. *Numerical Recipes 3rd Edition: The Art of Scientific Computing*, 3rd ed.; Cambridge University Press: New York, NY, USA, 2007.
26. Henry, E. R.; Hofrichter, J. *Methods Enzymol.* **1992**, *210*, 129–192.
27. Panman, M. R. Observing invisible machines with invisible light: The mechanics of molecular machines. Ph.D. thesis, University of Amsterdam, 2013.
28. Marcu, L.; French, P. M.; Elson, D. S. *Fluorescence lifetime spectroscopy and imaging: principles and applications in biomedical diagnostics*; CRC Press, 2014.
29. Muller, M. *Introduction to confocal fluorescence microscopy*; SPIE press, 2006; Vol. 69.
30. Kirshner, H.; Aguet, F.; Sage, D.; Unser, M. *J. Microsc.* **2013**, *249*, 13–25.
31. Resolution and Contrast in Confocal Microscopy (15.01.2017.). `http://www.olympusmicro.com/primer/techniques/confocal/resolutionintro.html`.

32. Otsu, N. *Automatica* **1975**, *11*, 23–27.
33. FLIM ROI Fitting (15.01.2017.). `http://www.tcspc.com/doku.php/howto:roi_fitting_using_the_flim_script`.